DOI: 10.1002/ejic.201100186

Proton Conductivity versus Acidic Strength of One-Pot Synthesized Acid-Functionalized SBA-15 Mesoporous Silica

Nicolas Bibent,[a,b] Ahmad Mehdi,[a] Gilles Silly,[a] François Henn,[a] and Sabine Devautour-Vinot*[a]

Keywords: Self-assembly / Hybrid materials / Organic-inorganic hybrid composites / Mesoporous materials / Conducting materials

This paper reports on the one-pot synthesis and characterization of the functionalized mesoporous SBA-15 silica, which contains two loadings of the different acid groups [CO_2H, $PO(OH)_2$ and SO_3H]. The thermodynamic features of the water that was confined in these porous silicas was investigated by Differential Scanning Calorimetry (DSC). The results showed that the melting behaviour of the confined water was mainly governed by the pore diameter and, as a consequence, indicated that the chemical "decoration" of the porous surface did not play a key role in the water thermodynamics. On the contrary, the proton conductivity of the hydrated mesoporous materials, which was examined under a wide range of temperatures (–100 to 70 °C), was strongly dependent on both the physical state of the confined water and the acidity of the functional groups that were located at the porous surface. The proton conductivity was shown to be directly related to the pK_a and the density of the functional groups attached to the mesopore surface. The high conductivity values that were obtained at a low temperature when the confined water is frozen, led us to postulate that the SO_3H-functionalized SBA-15 sample could be a promising candidate for electrolyte solid applications in fuel cells.

Introduction

Organic-inorganic hybrid materials that are based on silica and that are obtained by the sol-gel process have attracted considerable attention during the past few decades as they constitute a unique class of materials that combines the properties of the organic moieties and the inorganic matrices.[1–3] Since the discovery of ordered mesoporous silicas,[4–7] many investigations have focused on their functionalization in order to render them suitable for applications such as catalysis, separation, chemical sensors and so forth. Two main approaches have been used to anchor the organic groups onto the inner pore surface of the mesoporous silicas: the grafting method (post synthesis) and the co-condensation method (direct or one-pot synthesis). The post synthesis grafting of an organotrialkoxysilane $RSi(OR')_3$ onto the inner pore surface of the mesoporous silica was the first method established for functionalization.[8–10] This method is generic and allows for the incorporation of many R groups, including bulky ones. However, neither the loading nor the surface distribution of the functional groups, which depends on several parameters such as the number of residual silanol (SiOH) groups as well as their accessibility, are easily controlled by this synthetic route.[11,12] Furthermore, post synthesis grafting also makes the functionalization of the outer surface of the materials possible. A one-step alternative approach, which overcomes the main restrictions of the post synthesis method, has been developed.[11,13,14] It consists of the copolymerization of tetraethyl orthosilicate (TEOS) and an organotrialkoxysilane, $RSi(OR')_3$, in the presence of a structure-directing agent. This method requires that the R group is sufficiently hydrophobic to enter the core of the micelle and not so bulky that it disturbs the self-assembly imposed by the structure-directing agent. The main advantages of this method are that the functional groups are located at the inner surface of the material, their density is very well controlled and they are homogeneously distributed along the pores.[14] The drawbacks are that the size of the micelle and, consequently, the pore diameter are affected by the functional groups. Although the porous structure is maintained, the textural properties may vary slightly from one sample to another.

Among the numerous mesoporous organic-inorganic hybrid solids, efforts have been done to prepare acid-functionalized mesostructured porous silica materials that can be used as solid electrolytes.[15–22] The acid-functionalized mesoporous materials (by grafting or co-condensation) constitutes a promising class of solid-state, intermediate-temperature, proton conductors, which are dedicated to Proton Exchange Membrane Fuel Cells (PEMFCs), due to their

[a] Institut Charles Gerhardt Montpellier, UMR 5253, Université Montpellier II,
Place E. Bataillon, 34095 Montpellier Cedex 5, France
Fax: +33-4-67144290
E-mail: devaut@lpmc.univ-montp2.fr
[b] Institut de Chimie Séparative de Marcoule (ICSM) UMR 5257(UM2/CNRS/CEA/ENSCM),
30207 Bagnols sur Cèze, France

Supporting information for this article is available on the WWW under http://dx.doi.org/10.1002/ejic.201100186.

high charge carrier concentration, adjustable acid group density, oxidation resistance, thermal stability and high water adsorption properties in relation to both their high surface area and porous volume. By analogy with the renowned Nafion proton-conducting membrane, many studies focussed on sulfonic acid functionalization.[15–19,22] Alternatively, mesoporous silica proton conductors that are based on phosphoric or phosphonic acids have also attracted attention.[20,21] Owing to the amphoteric nature of the phosphonic acid, such solids can behave as both a proton donor (acidic) and a proton acceptor (basic) to form dynamic hydrogen bond networks in which the protons are readily transported by the rapid breaking and forming of the hydrogen bonds,[20,23,24] which occurs even at low humidity and intermediate temperatures (i.e., 100 to 150 °C). Even if the proton conduction properties for each type of these materials has been clearly demonstrated, it remains difficult to highlight the most promising candidate for the PEMFCs application since the comparison between their conductivity performances is not straightforward. These materials differ from one another not only in the nature of the acid group, but also by other parameters, such as the synthesis mode, the acid group density, the pore diameter and so forth.

In this study, we reported on the synthesis and the conductivity properties of the mesoporous SBA-15 silica that was functionalized by different acid groups [CO_2H, $PO(OH)_2$ and SO_3H] for two densities of functionalization. All of the materials were prepared by direct synthesis by using P123 as the structure-directing agent. The porous structure was characterized by nitrogen adsorption-desorption isotherms, small angle X-ray Diffraction (XRD) and Transmission Electron Microscopy (TEM). The local structure of the functionalized SBA-15 was checked by means of a solid-state NMR spectroscopy study. The ^{29}Si nucleus was used in order to probe the silica network whilst the ^{13}C and ^{31}P nuclei allowed us to examine the local structure of the functional groups. Before addressing the conductivity properties of the hydrated samples, the thermodynamic properties of the water molecules, which were confined in the mesoporous material, were investigated by using Differential Scanning Calorimetry (DSC). The proton conductivity was then measured by means of Complex Impedance Spectroscopy and the data was discussed in terms of the nature and concentration of the protogenic group of the functionalized mesoporous silica. In this paper we chose to investigate the functionalized SBA-15 samples that were prepared by the one-pot synthesis route, despite the fact that the textural properties are of lower quality compared to that of the "homologous" materials that are prepared by post synthesis grafting, since it offers much better control over the inner surface chemistry (i.e., the functionalization rate as well as the function accessibility and distribution). Moreover, the d.c. conductivity of the fully hydrated porous solid state materials is not necessarily related to the textural characteristics of the surface chemistry. For the reasons mentioned above, the one-pot synthesis route was more appropriate for the systematic investigation into the hydrated sample conductivity as a function of the nature and loading of the acid groups.

Results and Discussion

Preparation and Characterization of the Acid Functionalized SBA-15 Silica Materials

The unfunctionalized SBA-15: The unfunctionalized SBA-15 was prepared as described previously[25] by the hydrolysis and polycondensation of tetraethoxysilane (TEOS) in the presence of Pluronic 123 as the structure-directing agent. After aging and the removal of the surfactant, the solid product was dried and denoted as SBA-15.

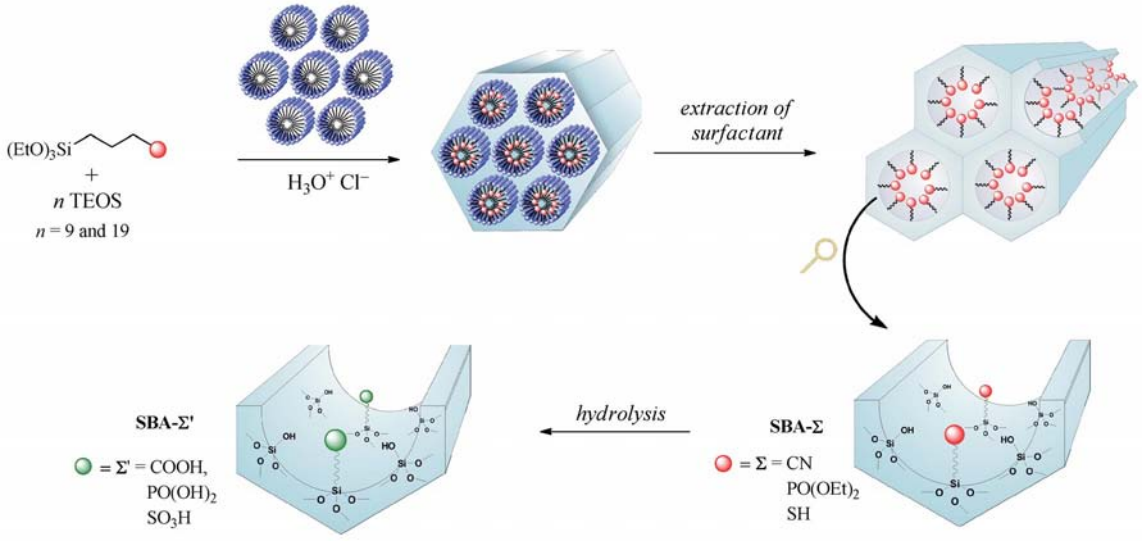

Scheme 1. The preparation of the acid-functionalized materials, SBA-CO_2 H, SBA-$PO(OH)_2$ and SBA-SO_3H.

The acid-functionalized SBA-15: The propylphosphonic, propylsulfonic or propylcarboxylic acid-functionalized SBA-15 materials were obtained by hydrolysis (by refluxing in an acidic aqueous solution) of the functionalized mesoporous materials that contained the $PO(OEt)_2$, SH or CN groups, respectively, and that had been previously prepared by a one-pot co-condensation of the Pluronic 123 with a mixture of $[(EtO)_3Si(CH_2)_3–X]$ and TEOS, where X = $PO(OEt)_2$, SH or CN, respectively (see Scheme 1). The $[(EtO)_3Si(CH_2)_3–X]/n$TEOS (with n = 9, 19) molar ratio was fixed at 1/9 or 1/19 in order to obtain materials that had two different loadings of the acid functionalities.[26,27,28] The samples were labelled SBA-$PO(OH)_2$ (1/9), SBA-$PO(OH)_2$ (1/19), SBA-SO_3H (1/9), SBA-SO_3H (1/19) and SBA-CO_2H (1/9). The functionalization of these materials was verified by NMR spectroscopy.

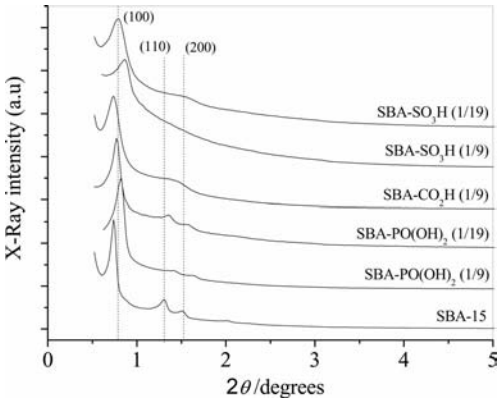

Figure 1. The XRD patterns for SBA-15 and the different acid-functionalized silica samples (the XRD patterns are shifted by a constant factor).

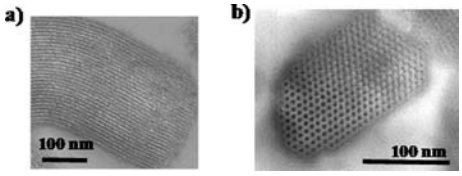

Figure 2. The TEM micrographs of SBA-CO_2H (1/9). (a) The horizontal and (b) the perpendicular views.

X-ray Diffraction

The small angle powder X-ray pattern of the unfunctionalized SBA-15 is depicted in Figure 1. It exhibited one intense peak that was accompanied by two weak peaks, which were indexed to the (100), (110) and (200) diffractions plans, respectively, in the *P6mm* space group. This X-ray pattern is typically observed for materials that are characterized by a hexagonal-ordered array of a one-dimensional channel structure.[29] For the functionalized SBA-15 samples (cf. Figure 1), the main (100) peak remained, while the others were more or less pronounced depending on the nature and on the concentration of the functional group. However, it has been shown that materials with a similar single reflection can still exhibit local hexagonal symmetry.[30] In addition, the Transmission Electron Microscopy images (TEM) provided evidence of the highly ordered hexagonal structure of the porous network (cf. Figure 2, and Figure S1 in the Supporting Information).

The d_{100} spacing and the a unit cell parameter ($a = 2d_{100}/\sqrt{3}$) values are summarized in Table 1. The cell parameter of the acid-functionalized SBA-15 materials decreased compared to that of SBA-15, except for SBA-CO_2H (1/9). It is worth noting that this decrease was more pronounced when the degree of functionalization was increased. This implies that the precursors $[(EtO)_3Si(CH_2)_3$-$PO(OEt)_2]$ and $[(EtO)_3$-$Si(CH_2)_3$–SH] slightly disturbed the stability of the micelles during the one-pot synthesis of the functionalized silica and that this perturbation is proportional to the precursor concentration.

N_2 Adsorption–Desorption Measurements

The N_2 adsorption–desorption isotherms of the dry unfunctionalized and functionalized SBA-15 samples are illustrated in Figure 3. According to the IUPAC classification, all of the samples [except for SBA-SO_3H (1/9), cf. Figure S2 in the Supporting Information] exhibited a type IV isotherm. These typical isotherms are characterized by a hysteresis loop of the H_1 type and by the sharp adsorption and desorption branches in relation to a narrow pore size distribution. The position of the capillary condensation step is directly related to the pore diameter, which varies with the nature (size, polarity and lipophilic character) of the functional group, because of its influence on the micelle size

Table 1. The structural and textural properties of dry SBA-15 and the different acid-functionalized silica samples. The ΔT_m values that were obtained from the DSC experiments have also been added.

Sample	Textural data (N_2 adsorption–desorption)					Structural data (XRD)		DSC data
	S_{BET} [$m^2 g^{-1}$]	$V_{\mu\text{-pore}}$ [$cm^3 g^{-1}$]	V_{pore} [$cm^3 g^{-1}$]	D_{p1}(BJH$_{des}$) [Å]	D_{p2} (4V/S) [Å]	d_{100} [Å]	A [Å]	ΔT_m [K]
SBA-15	634	0.02	1.30	82	82	119	137	–8.1
SBA-$PO(OH)_2$ (1/9)	540	0.01	1.03	66	76	109	126	–10.6
SBA-$PO(OH)_2$ (1/19)	518	0.01	1.23	79	95	116	134	–7.9
SBA-SO_3H (1/9)	770	0.04	0.49	51	25	103	119	–17.3
SBA-SO_3H (1/19)	830	0.002	0.91	66	44	112	129	–12.7
SBA-CO_2H (1/9)	625	0.001	1.32	80	84	119	137	–8.0

during the one-pot synthesis. In the case of the SBA-SO_3H (1/9) sample, the hysteresis loop is a composite of the H_1 and H_2 types (cf. Figure S2), which suggested that some constrictions are present along the nanopore. As a consequence, the capillary condensation occurred in a broader domain of relative pressure and the desorption branch exhibits a step due to the "pore-blocking" effect.[31–33] This complex porous structure was most probably due to the influence of the organosilicon precursor as a result of its hydrophilicity and its compatibility with the micellar structure.

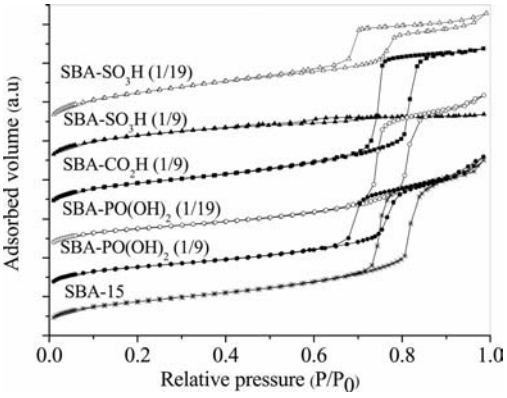

Figure 3. The nitrogen adsorption and desorption isotherms for SBA-15 and the different acid-functionalized silica samples (the isothermal plots are shifted by a constant factor).

It was concluded that the mesoporous structure is maintained regardless of the functionalization. The nitrogen capillary condensation of the functionalized samples shifted towards a lower relative pressure compared to that of SBA-15, which meant that the textural properties of the silica depend on the concentration, as well as on the nature, of the functionalization. The textural data (i.e., the surface area and pore volume) obtained for all of the samples are listed in Table 1. The external surface areas and the pore wall thicknesses are given in Supporting Information (III, cf. Table S3). The data for SBA-15 were in good agreement with those that have been reported for silica that exhibits similar pore diameters.[29,34] In all of the cases, the microporosity ($< 0.05\ cm^3\ g^{-1}$) was negligible compared to that of the pore volume. The pore diameter (D_{p1}) of the functionalized samples decreased with the increase in the concentration of the organic groups. By contrast, the evolution of the textural properties [specific area (S_{BET}) and porous volume (V_{pore})] with the nature of the functional group is relatively complex and no clear trend was observed. The different textural properties of the obtained materials were due to the different types of interactions between the molecular precursors and the micelles during the synthesis. Therefore, a comparison between the textural properties that is based on the nature of the functionalization is not straightforward. In addition, the arrangement and the steric environment of the organic chains at the nanopore surface may play a key role. This last point is emphasized when the pore diameter obtained from the BJH method (D_{p1}) is compared with the dynamic diameter (D_{p2}), which was extracted from the ratio of the pore volume (V_{pore}) and the specific area (S_{BET}) (i.e., $D_{p2} = 4V_{pore}/S_{BET}$). There is a fairly good agreement between both of the diameter values for SBA-15 and SBA-CO_2H (1/9) (see Table 1), whereas a discrepancy occurred for the two other families of samples SBA-$PO(OH)_2$ and SBA-SO_3H, in which the discrepancy was more marked as the organic chain concentration increased. For these two last samples, the cylindrical pore model is probably not acceptable. This outcome was probably due to the orientation of the chains and/or the assembly at the pore surface by means of hydrogen bonds between either the functional groups or the functional groups and the surface.[35] However, for the hydrated samples, the inter-function and surface-function bonds are inhibited,[35] hence, this point was not relevant in this study since the conductivity properties of the hydrated functionalized SBA-15 materials were analyzed.

Solid-State NMR Characterization

The ^{29}Si single-pulse NMR spectra of the dry samples of SBA-15 and the functionalized SBA-15 materials are presented in Figure 4. The silicon atoms are located at the centre of the oxygen tetrahedra that are connected at the corners. The silica network could be described by using the common nomenclature in terms of Q^n $Si(OSi)_n(OH)_{4-n}$, where n = 0, 1, 2, 3 or 4, and T^m $RSi(OSi)_m(OH)_{3-m}$, where m = 0, 1, 2 or 3 sites, which differ in the number of organic radical and OH groups that are connected to the tetrahedron. Our samples showed evidence of two line groups: the organosiloxane T^m lines and the siloxane Q^n lines, which were spread in the range of –50 to –80 ppm and –80 to –120 ppm, respectively. The positions, relative intensities and assignment of the lines are reported in Table 2. The T^m lines were observed only for the functionalized samples. The T^3 line was always present and corresponded to the silicon atoms that are connected to the propyl spacer of the functional groups.

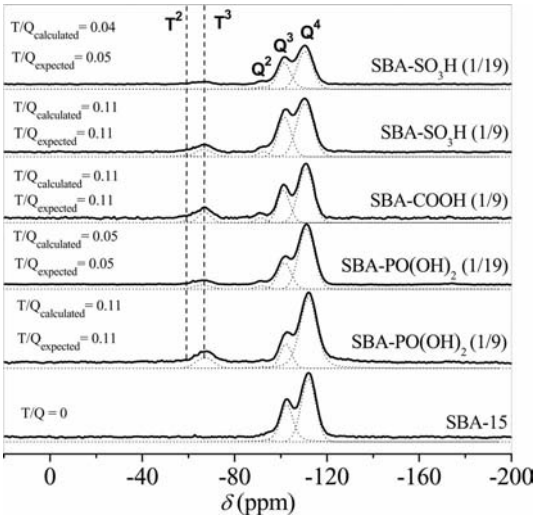

Figure 4. The ^{29}Si single-pulse solid-state NMR spectra for SBA-15 and the functionalized SBA-15 samples.

Table 2. The deconvolution data of the ^{29}Si NMR spectra for the dry SBA-15 sample and the different acid-functionalized silica samples. δ [ppm] and R.I. [%] are the isotropic chemical shift and the relative integrated intensity, respectively.

Sample	Parameters	T^2	T^3	Q^2	Q^3	Q^4	Ratio T^m/Q^n
SBA-15	δ			–93	–103	–112	0
	R.I.			1	37	62	
SBA-$PO(OH)_2$ (1/9)	δ		–67	–92	–102	–112	0.11
	R.I.		10	1	15	74	
SBA-$PO(OH)_2$ (1/19)	δ		–66	–92	–102	–111	0.05
	R.I.		5	3	25	67	
SBA-CO_2H (1/9)	δ	–59	–67	–91	–101	–111	0.11
	R.I.	1	9	1	28	61	
SBA-SO_3H (1/9)	δ	–58	–67	–93	–102	–111	0.11
	R.I.	2	8	1	34	55	
SBA-SO_3H (1/19)	δ		–66	–92	–102	–111	0.05
	R.I.		4	2	38	56	

Three distinct resonances for the siloxanes were observed and were associated to the Q^2, Q^3 and Q^4 sites. The relative integrated intensities of the lines indicated that the majority of the silicon atoms belong to the Q^4 substructures (Table 2), which correspond to the silicon atoms located in the walls. The Q^2 and Q^3 sites indicated that the silanol groups were mainly located at the surface of the porous samples. The Q^2 sites were rarely present with a concentration of only a few percent. According to the ^{29}Si NMR results, the presence of the T^m peaks, where the T^3 sites were predominant over the T^2 sites, confirmed that the organosilane precursors were effectively condensed as a part of the silica matrix.[36] From the relative integrated intensities of the Q^n and T^m signals for all of the functionalized samples, the T^m/Q^n ratio was estimated to be 0.11 and 0.05 for the 1/9 and 1/19 loading of the acid functionalities (Table 2), respectively. These results are in very good agreement with the molar composition of the initial mixtures [1 $(EtO)_3Si$-$(CH_2)_3$–X]/*n* TEOS (*n* = 9, 19), where X = $PO(OEt)_2$, SH or CN.

The NMR spectra of the hydrated samples (not shown) were also recorded and did not exhibit significant differences. Hence, it was concluded that the silica wall is not reactive to water in this case.

The ^{13}C CP/MAS NMR spectra of the dry samples that are presented in Figure 5 and the NMR parameters that are reported in Table 3 enabled us to check that the one-pot functionalization, as well as the hydrolysis of the obtained solids, were successfully achieved for all of the samples. Furthermore, it was clearly demonstrated by the disappearance of the bands assigned to the CN, O–CH_2–CH_3 and CH_2–SH functionalities of the SBA–CO_2H (1/9), SBA–$PO(OH)_2$ (1/9) and SBA–SO_3H (1/9) samples, respectively, that no unreacted functional groups remained in the studied samples. Moreover, the SBA–CN (1/9), SBA–$PO(OEt)_2$ (1/9) and SBA-SH (1/9) spectra showed a line at δ = 59 ppm that was attributed to the residual ethoxy groups of TEOS or the precursor. This line disappeared following the chemical modification (hydrolysis) of the CN, $PO(OET)_2$ and SH groups. The data that was obtained for the solids that are characterized by a lower functional group density presented the same trends (not shown here). The ^{13}C CP-MAS experiments were not acquired for the hydrated samples because, in the presence of water, cross polarization is much less efficient, which leads to noisy spectra.

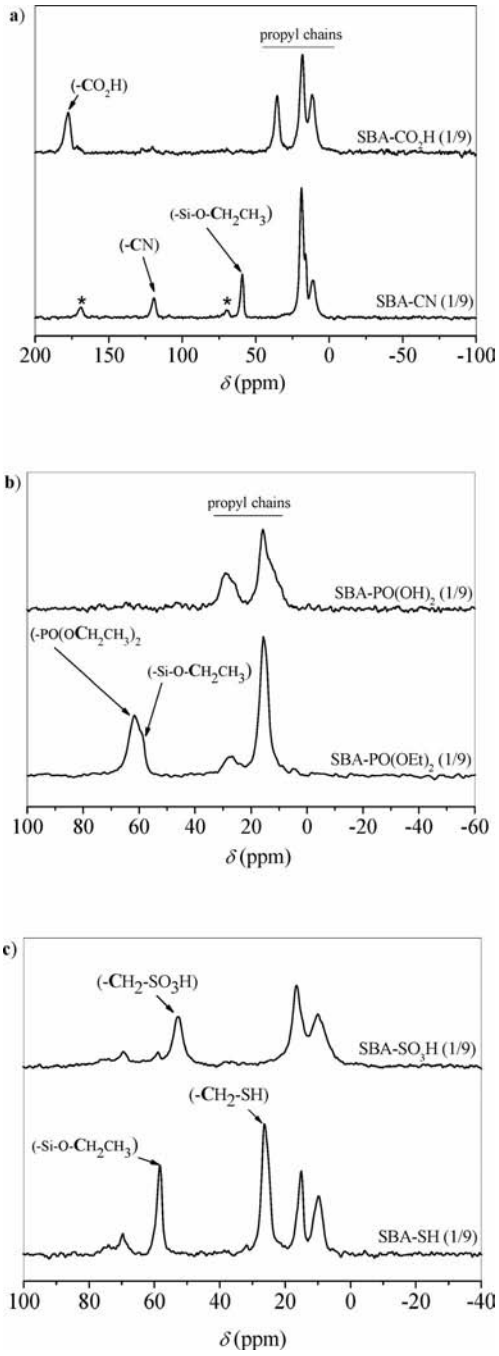

Figure 5. The ^{13}C CP/MAS solid state NMR spectra of: (a) SBA-CN (1/9) and SBA-CO_2H (1/9); (b) SBA-$PO(OEt)_2$ (1/9) and SBA-$PO(OH)_2$ (1/9); (c) SBA-SH (1/9) and SBA-SO_3H (1/9).

Table 3. The assignment of the experimental chemical shifts values of the ^{13}C CP/MAS solid state NMR to the specific chemical species for the SBA-CN (1/9), SBA-CO_2H (1/9), SBA-$PO(OEt)_2$ (1/9), SBA-$PO(OH)_2$ (1/9), SBA-SH (1/9) and SBA-SO_3H (1/9) samples.

Sample	δ (ppm)	Species	Ref.
SBA-CN (1/9)	11	Si-**C**H_2(CH_2)$_2$-CN	[37–40]
	16	Si-O-CH_2-**C**H_3	
	19	Si-CH_2-**C**H_2-CH$_2$-CN	
	59	Si-O-**C**H_2-CH_3	
	120	Si-(CH_2)$_3$-CN	
SBA-CO_2H (1/9)	11	Si-**C**H_2(CH_2)$_2$-CO_2H	
	19	Si-CH_2-**C**H_2-CH$_2$-COOH	
	36	Si-(CH_2)$_2$-CH_2-CO_2H	
	178	Si-(CH_2)$_3$-CO_2H	
SBA-$PO(OEt)_2$ (1/9)	10-20	Si-CH_2-**C**H_2-CH$_2$-P-	[26,35,41]
	10-20	Si-O-CH_2-**C**H_3	
	10-20	Si-(CH_2)$_3$-PO(OCH_2CH_3)$_2$	
	30	Si-(CH_2)$_2$-CH_2-P-	
	59	Si-O-**C**H_2-CH_3	
	63	Si-(CH_2)$_3$-PO(O**C**$H_2$$CH_3$)$_2$	
SBA-$PO(OH)_2$ (1/9)	10-20	Si-CH_2-**C**H_2-CH$_2$-P	
	30	Si-(CH_2)$_2$-CH_2-P-	
SBA-SH (1/9)	10	Si-**C**H_2(CH_2)$_2$-SH	[41,42]
	15-20	Si-CH_2-**C**H_2-CH$_2$- SO_3H	
	15-20	Si-O-CH_2-**C**H_3	
	26	Si-(CH_2)$_2$-CH_2-SH	
	59	Si-O-**C**H_2-CH_3	
SBA-SO_3H (1/9)	10	Si-**C**H_2(CH_2)$_2$-SO_3H	
	17	Si-CH_2-**C**H_2-CH$_2$-SO_3H	
	53	Si-(CH_2)$_2$-CH_2-SO_3H	

The ^{31}P NMR spectra for SBA-$PO(OEt)_2$ and SBA-$PO(OH)_2$ are shown in Figure 6. The ^{31}P spectrum for the dry SBA-$PO(OEt)_2$ exhibited only one line, located at δ = 34 ppm, which indicated a homogeneous environment for the phosphonate groups.[35] The spectrum for SBA-$PO(OH)_2$, however, showed two lines. According to Aliev et al.,[35] the signal at δ = 33 ppm can be attributed to free phosphonic acid groups and that at δ = 23 ppm can be attributed to phosphonic acid groups that are engaged in hydrogen bonds. For the hydrated SBA-$PO(OH)_2$ sample, we observed that the line narrowed and that a slight shift occurred towards a lower chemical shift value compared to that reported for the dry SBA-$PO(OH)_2$ sample. The narrowing of the line width emphasized that the mobility of the functional groups increased upon water adsorption. Moreover, for the hydrated SBA-$PO(OH)_2$ sample, we observed that the line corresponding to the phosphonic groups that are engaged in hydrogen bonds is greatly reduced. This indicated that these hydrogen bonds are unstable when the water molecules are adsorbed in the nanopores.

The data obtained for the solids with the lower functional group density presented the same trends (not shown here). These results, together with those obtained from the ^{13}C NMR spectra, highlighted that the hydrolysis of SBA-$PO(OEt)_2$ was successfully achieved.

Properties of the Confined Water

The first step in our experimental investigation consisted in characterizing the thermodynamics of the water molecules that were confined in the nanopores of our samples, since the conductivity properties of the functionalized samples are strongly dependent on the physical state of the water, as we shall see later. The thermodynamics was characterized by using Differential Scanning Calorimetry (DSC) measurements. The DSC signals that were obtained upon heating are shown in Figure 7 for all of the samples. As expected,[43,44] they exhibit two endothermic peaks. The first one, which occurs below 0 °C, corresponds to the melting of the solid state water that was confined in the SBA-15 nanopores. The second one, which is located between 70 and 100 °C, is related to the water desorption. In both cases, the peak position depends on the nature of the functionalized silica. As is usually observed for confined fluids, both the melting and desorption of the water occurred over a large temperature range. The melting occurred in a temperature range that is lower than that of bulk water, whatever the surface decoration, which is in agreement with that reported for functionalized SBA-15 or MCM-41.[43–49] Table 1 lists the melting temperature shifts ΔT_m, with $\Delta T_m = T_m - 273$ K where T_m is the temperature at the peak extremum. One may wonder if ΔT_m is influenced by either the chemical nature of the functionalized surface or the pore diameter since it differs from one sample to another. Ac-

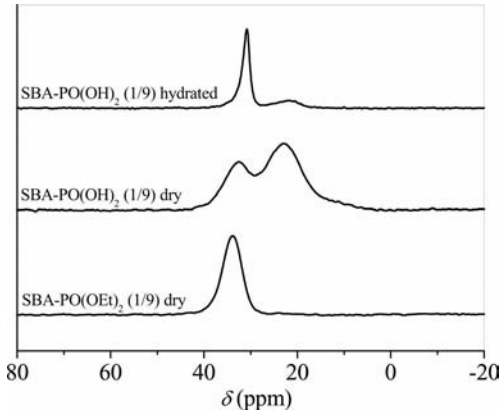

Figure 6. The ^{31}P single-pulse solid-state NMR spectra of the dry SBA-$PO(OEt)_2$ and SBA-$PO(OH)_2$ samples and of the hydrated SBA-$PO(OH)_2$ sample.

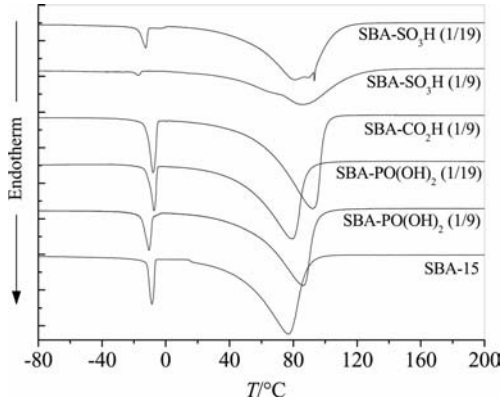

Figure 7. The DSC scanning curves that show the melting and boiling peaks of the water that is confined in the SBA-15 sample and the different acid-functionalized silica at complete pore filling. (The DSC curves are shifted by a constant factor).

cording to the Gibbs–Thompson equation [Equation (1)], a linear relationship between ΔT_m and the inverse of the pore radius (R_p) is established.[50]

$$\Delta T_m = -C_{GT}/R_p \text{ with } C_{GT} = 2T_0(\gamma_{WS} - \gamma_{WL})\cdot v/\Delta h_{SL} \quad (1)$$

C_{GT} is the Gibbs–Thompson constant, which accounts for the surface free energies per unit area of the interfaces wall/solid (γ_{WS}) and wall/liquid (γ_{WL}), the molar melting enthalpy (Δh_{SL}) and the molar volume (v) of the liquid or solid phase, depending on which has the lower free energy at the wall surface. As has been reported,[51] Equation (1) can be expressed by Equation (2), where R_t represents the thickness of the liquid-like layer at the wall surface and at the relevant melting temperature.

$$\Delta T_m = -C_{GT}/R_s \text{ with } R_s = R_p - R_t \quad (2)$$

This distance corresponds to approximately two monolayers of water molecules[51,52] and was estimated to be 0.6 nm. Therefore, R_s can be seen as the solid core radius. Jähnert et al.[51] investigated unfunctionalized silica and thus excluded the potential role that is played by the chemical surface. In our case, the inner surface differed from one sample to another because of the presence of the functional groups. This chemical decoration may influence the fluid/pore interaction and hence the melting point of the confined fluid. We assumed that in our case R_p could be estimated from the nitrogen adsorption/desorption isothermal analysis by means of the BJH formalism and hence we plotted the ΔT_m experimental values (see Table 1) as a function of R_s^{-1} in order to check whether or not Equation (2) was obeyed. The linear dependence of ΔT_m is evident in Figure 8 and the corresponding C_{GT} parameter (C_{GT} = 33 K nm), as determined from the linear fitting procedure, was in perfect agreement with the one reported by Brun et al. (32.33 K nm).[53] In addition, the negligible deviation found at the origin coordinate (i.e., 0.95 K) was considered to fall within the experimental error. Therefore, it was assumed that Equation (2) accounts well for the experimental data and, hence, it was concluded that the effect of the chemical nature of the inner pore surface on the water solid/liquid transition process is negligible.[54]

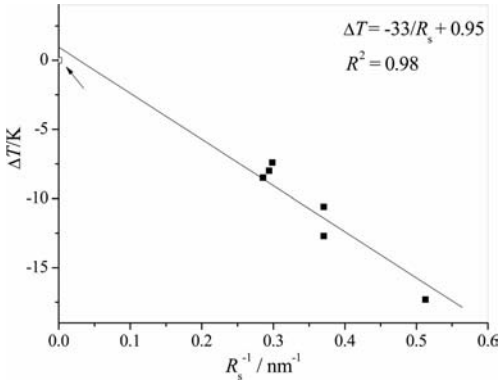

Figure 8. The melting point depression ΔT_m vs. the inverse of the core radius R_s, see Equation (2). The line shows the fit of the data to a R_s^{-1} relation. The point that corresponds to the bulk water melting is also represented by the open square symbol that is indicated by the arrow.

Proton Conductivity Properties

Complex Impedance Spectroscopy (CIS) has been used extensively to address the dynamics of confined liquids.[55–57] In this work, we first studied the conductivity response of all of the dehydrated SBA-15 samples since, as reported in ref.[56] the dynamics of the silanol groups at the inner surface of the nanopores give rise to a dielectric relaxation, which is associated to the rotational motion of the polar O–H bond. However, for all of our samples, neither dielectric relaxation nor d.c. conductivity was observed in the temperature and frequency ranges considered. These results showed that the reorientational motions of the OH groups were too fast or too slow to be detected by using our experimental conditions and that there was no electrical charge (electrons or ions) that diffused into the core or at the surface of the dehydrated samples. On the contrary, all of our hydrated samples exhibited both polarization [$\sigma_{pol}(\omega)$] and d.c. conductivity (σ_{dc}) signals [cf. Equation (7) and Exp. Section]. This is clearly illustrated in Figure 9, where the global conductivity (σ_{ac}) was recorded at different temperatures as a function of the frequency of the applied electrical field for SBA-PO(OH)$_2$ (1/9), which can be taken as a typical example. At the highest temperatures and lowest frequencies, it was observed that the hydrated samples exhibit a so-called Maxwell–Wagner–Sillars contribution [$\sigma_{MWS}(\omega)$] that is due to interfacial polarization that arises from the blocking of the ionic charges at the sample/metallic electrode interface. As a result of the comparison between their behaviour and that of their dehydrated counterpart, it can be assumed that the a.c. conductivity of the hydrated samples is due to the water that is confined inside the nanopores.

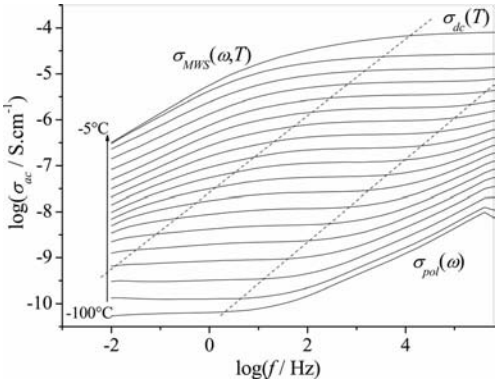

Figure 9. The real part of the global conductivity σ_{ac} as a function of the frequency, f, for the water that is confined in SBA-PO(OH)$_2$ (1/9) at different temperatures, which range from –100 to –5 °C, by steps of 5 °C.

The values for the d.c. conductivity, which was determined from the a.c. conductivity spectra (see Figure 9), were plotted as a function of the inverse temperature that

followed the relation deduced from the Nernst–Einstein model for ionic diffusion [Equation (3)].

$$\sigma_{dc}(T) = \sigma_0/T \cdot \exp(-E_a/kT) \quad (3)$$

σ_0 is the d.c. conductivity at infinite temperature, E_a is the activation energy and k is the Boltzmann constant. As shown in Figure 10, three regimes were identified within the corresponding temperature ranges: (I) –100 °C < T < –10 °C, (II) –10 °C < T < 40 °C and (III) T > 40 °C. These temperature domains correspond to the existence of the different phases of the confined water, which were identified from the DSC experiments: the confined water is frozen in (I), in a liquid state in (II) and evaporates in (III). This close connection between the behaviour of the d.c. conductivity and the DSC experiments was further validated by the fact that the transition between the domains (I) and (II) occurs at a temperature very close to the melting temperature, T_m, obtained from the DSC experiments. This outcome, which was reported for SBA-PO(OH)$_2$ (1/9), has been observed for all of the samples. As already outlined, this undoubtedly suggests that the d.c. conductivity of our mesoporous silica strongly depends on the presence of water and on its physical state. The decrease in the d.c. conductivity that was measured in domain (III), which corresponds to the desorption of the confined water molecules, confirmed this assumption. The system obeys Equation (3) in domains (I) and (II) as is shown by the linear dependence that is seen in Figure 10. In domain (II) we observed a decrease in the slope (i.e., the activation energy) compared to that of domain (I), which is in relation to the higher mobility of the charge carriers in the liquid phase of the water. Although Equation (3) appears to be valid in domain (II), no activation energy value could be determined due to the narrowness of the temperature domain in which it was estimated. The calculation of the activation energy was possible in domain (I) for all of the investigated samples (Figure 10 and Table 4). It was not possible to clearly distinguish the influence of the acid group nature and its density from the E_a values obtained for the different samples. However, it should be emphasized that all of these values fall within the same order of magnitude as that reported for the solid state water that was confined in MCM-41 (E_a = 0.6 eV)[56] or for bulk water (E_a = 0.6 eV).[57] This comparison strongly suggested that the conduction mechanism involved in our systems is connected to the proton dynamics in frozen water[60,61] and led us to consider that the d.c. conductivity is probably due to the diffusion of protons that is assisted by water molecules by means of a Grotthuss mechanism.[62–64] In this model, the transport of protons is caused by the translocation of protons from one water molecule to its neighbour, followed by a subsequent rotation of the water molecules. The latter governs the conductivity mechanism and, hence, the activation energy. For the unfunctionalized SBA-15 sample, the protons that participate in the Grotthuss mechanism probably originate from the water molecules themselves but also from the dissociation of the silanol groups present at the nanopore surface.[65] For the functionalized samples, a larger quantity of mobile protons can be generated by the dissociation of the acid functionalities. The Grotthuss mechanism was confirmed by the fact that the E_a values for the d.c. conductivity, which was reported for all of the samples, were almost independent of the origin and content of the protons (Table 4). σ_{dc} is, therefore, more influenced by the intrinsic dynamics of the water molecules than by the acidity of the surface and, hence, is not very dependent on the functional groups. This suggests that the proton transport in these fully hydrated samples is mainly governed by the water molecule dynamics at the mesopore centre. The surface roughness thus plays a minor role, which is probably not the case for the dehydrated or weakly hydrated samples.

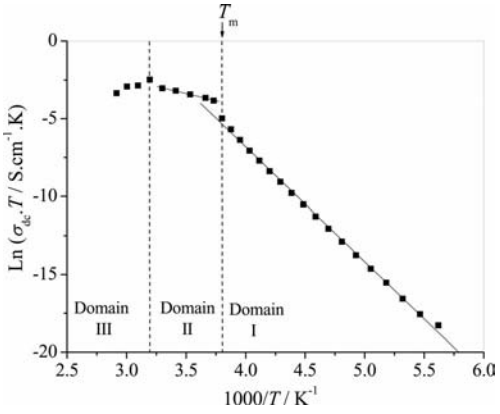

Figure 10. ln($\sigma_{dc} \times T$) vs. $10^3/T$ for the water that is confined in SBA-15-PO(OH)$_2$ (1/9). The lines are fits with the Nernst–Einstein equation.

Table 4. The activation energies for the diffusion part of the conductivity for the dry SBA-15 sample and the different acid-functionalized silica samples.

Sample	$\Delta E_a \pm 0.02$ [eV]
SBA-15	0.75
SBA-PO(OH)$_2$ (1/9)	0.65
SBA-PO(OH)$_2$ (1/19)	0.62
SBA-SO$_3$H (1/9)	0.68
SBA-SO$_3$H (1/19)	0.69
SBA-CO$_2$H (1/9)	0.65

Although the conductivity mechanism is most probably the same for all of the samples, the Arrhenius plots reported in Figure 11 show that the level of d.c. conductivity is much more sensitive to the surface chemistry. At a fixed temperature (e.g. T = –30 °C), the samples can be classified according to their d.c. conductivity: σ_{dc}[SBA-SO$_3$H (1/9)] > σ_{dc}[SBA-SO$_3$H (1/19)] > σ_{dc}[SBA-PO(OH)$_2$ (1/9)] > σ_{dc}[SBA-PO(OH)$_2$ (1/19)] > σ_{dc}[SBA-15] > σ_{dc}[SBA-CO$_2$H (1/9)]. Except for the SBA-CO$_2$H (1/9) sample, all of the functionalized silica exhibit higher d.c. conductivity values than that of SBA-15. This observation depends on both the loading of the functional groups and the nature of the acid groups. This suggests that the type of proton in the water that is confined at the pore centre, which depends on the functional group concentration as well as the strength of the acid functionalities, plays a key role in the level of the

d.c. conductivity. In fact, the mobile protons, which participate to the Grotthuss mechanism, mainly arise from the dissociation of the weak acids of the chain functionalities and/or the silanol groups. The d.c. conductivity is expressed by Equation (4).

$$\sigma_{dc} = n \cdot \mu \cdot q \quad (4)$$

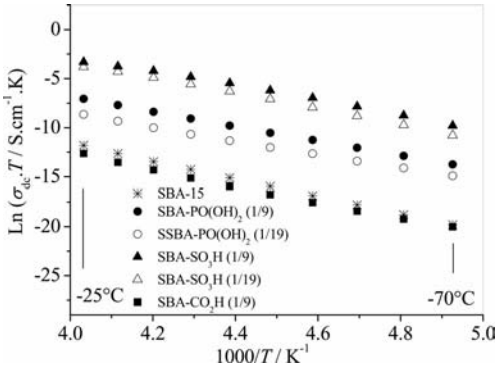

Figure 11. $\ln(\sigma_{dc} \times T)$ vs. $10^3/T$ for the water that is confined in SBA-15 and the different acid-functionalized silica in the temperature range of –70 to –25 °C.

n, μ and q are the density, the mobility and the electrical charge of the carrier, respectively. As emphasized by the activation energy values (Table 4), the proton mobility, μ, which is governed by the Grotthuss mechanism, can be considered as independent of the investigated sample. Therefore, provided that q is constant, it can be deduced that the magnitude of the d.c. conductivity is mainly governed by n, which is the density of the dissociated (i.e., mobile) protons in the water that is confined in the mesopores.

The density of the mobile protons can be readily estimated from the Brönstedt theory for a "weak" acid by using Equation (5).

$$-\log[H^+] = {}^1/_2 \cdot pK_a - {}^1/_2 \cdot \log[A]_0 \quad (5)$$

$[A]_0$ is the concentration of the weak acid and pK_a is its strength. Finally, provided that $n \propto [H^+]$ and that $[A]_0$ is the same for all of the (1/9) samples, Equations (4) and (5) can be combined to form Equation (6).

$$-\log(\sigma_{dc}) \propto pK_a \quad (6)$$

The evolution of $-\log(\sigma_{dc})$, which was recorded at –30 °C, as a function of the pK_a of the acid functional groups that decorated the nanopores of our samples is plotted in Figure 12. The pK_a values were collected from the literature,[66–68] except for that of the phosphonic acid groups for which no data could be found in the literature. In that case, we used the pK_a value that characterized the first acidity of the free propylphosphonic acid[69] as a first approximation. As demonstrated by the linear relationship that was observed in Figure 12, the experimental d.c. conductivity data is in perfect agreement with Equation (6) and, hence, validated the proposed assumption. Furthermore, this simple model enabled us to explain the lower d.c. conductivity level that was observed in the (1/19) samples, whose functional group loading is much lower than that of the (1/9) samples, and the lower d.c. conductivity of SBA-CO_2H (1/9) compared to that of SBA-15 in relation to its higher pK_a value. It is worth noting that the same trend was observed for all of the temperatures in domain I.

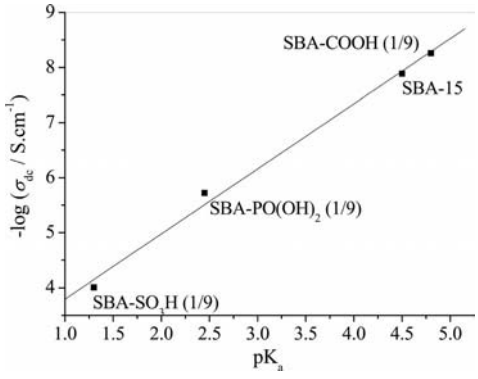

Figure 12. $-\log(\sigma_{dc})$ recorded at –30 °C vs. pK_a for the SBA-15 and the different acid-functionalized silica. The line shows the fit of the data to a direct pK_a relation.

Based on the d.c. conductivity values that were recorded at low temperature (i.e., –30 °C) (cf. Figure 12), and keeping in mind that in this case the confined water is frozen, the investigated samples and, in particular, SBA-SO_3H (1/9) could be considered to be reasonably good protonic conductors. In the latter case, the conductivity value recorded at –30 °C ($\sigma_{dc} = 10^{-4}$ S cm^{-1}) was even higher than that reported at 60 °C ($\sigma_{dc} = 2 \times 10^{-5}$ S cm^{-1})[17] for a similarly functionalized SBA-15, which was prepared by means of grafting, despite the fact that the operating conditions (i.e., temperature) in our case were rather unfavourable. In ref.[17] the data were recorded at 60 °C and in a 100% water-rich atmosphere, which means that the sample contained a large amount of liquid water. This may suggest that the increased order of the functional groups at the mesopore surface, which resulted from the one-pot synthesis, strongly enhances d.c. conductivity. In addition, Figure 12 also indicated that the best way to improve the d.c. conductivity of the functionalized SBA-15 samples consists in preparing solids with acid functionalities that are characterized by pK_a values that are lower than that of SBA-SO_3H (1/9). Thus, we propose to replace the propyl chain of this functionalized sample with a fluorinated or chlorinated counterpart. This should be favourable for making highly conductive solids that are potentially suitable for PEMFCs applications.

Conclusions

The mesoporous SBA-15 samples with the phosphonic, sulfonic or carboxylic acid functional groups were synthesized by the co-condensation method. Although the nature and the loading of these chemical "decorations" did not impact on the confined water thermodynamics, they did significantly influence the level of the proton conductivity of the fully hydrated solids. In this study, due to experimental limitations, the d.c. conductivity was investigated only while

the confined water was frozen ($T < -25$ °C). It was clearly demonstrated that the d.c. conductivity increases with the acidic strength and with the loading of the functional groups. A further investigation, in which the confined water is in the liquid state and in a controlled water atmosphere, was beyond the scope of this study. However, we predict that the d.c. conductivity will be much higher in this case. Therefore, we postulate that the d.c. conductivity values that were measured are high enough to suggest that these materials show promise for solid electrolyte applications. The d.c. conductivity measurements at a higher temperature and under various relative humidity conditions will be presented in a future paper.

Experimental Section

Chemicals: Pluronic P123 ($EO_{20}PO_{70}EO_{20}$, M = 5800 g/mol) and tetraethylorthosilicate (TEOS) were supplied by Aldrich and ABCR, respectively. Triethoxy(3-mercaptopropyl)silane [$(EtO)_3Si(CH_2)_3SH$] and (3-cyanopropyl)triethoxysilane [$(EtO)_3Si(CH_2)_3CN$] were supplied by Aldrich and were used as received. Diethyl [3-(triethoxysilyl)propyl]phosphonate [$(EtO)_3Si(CH_2)_3PO(OEt)_2$] was synthesized as described previously.[70]

Acid-Functionalized SBA-15: Pluronic P123 (8.0 g, 1.38 mmol) was dissolved in an aqueous solution of HCl (320 mL) (pH = 1.5). TEOS (16.8 g, 80.77 mmol) was added together with the appropriate amount of the selected precursor [$(EtO)_3Si(CH_2)_3$–X], which was chosen according to the nature and functional degree of the functionalized material that we required. This mixture was stirred until a clear solution was obtained and then NaF (0.08 g) was added. After stirring for 3 days at 60 °C, the resulting powder was filtered off and the surfactant was removed by Soxhlet extraction with hot ethanol for 24 h. The recovered solid was dried at 70 °C under vacuum. The obtained samples were denoted as SBA-$PO(OEt)_2$ (1/9), SBA-$PO(OEt)_2$ (1/19), SBA-SH (1/9), SBA-SH (1/19) and SBA-CN (1/9).

SBA-$PO(OEt)_2$ (1/9) (3.0 g, 3.90 mmol) or SBA-$PO(OEt)_2$ (1/19) (3.0 g, 2.18 mmol) was treated with aqueous HCl (50 mL, 12 N) while stirring at 100 °C over 24 h. The solid product was recovered by filtration, washed several times with water and ethanol and then dried at 70 °C under vacuum.[27,70] The prepared samples were denoted as SBA-$PO(OH)_2$ (1/9) and SBA-$PO(OH)_2$ (1/19).

For the propylsulfonic acid functionalized SBA-15 preparation, SBA-SH (1/9) (4.0 g, 5.99 mmol) or SBA-SH (1/19) (4.0 g, 3.16 mmol) was stirred with hydrogen peroxide solution (33%; 50 mL) over 24 h and was then treated with an aqueous solution of sulfuric acid (2 M; 25 mL) for 20 min. The solid products, SBA-SO_3H (1/9) and SBA-SO_3H (1/19), respectively, were recovered by filtration, washed several times with water and ethanol and then dried at 70 °C under vacuum.[27]

Propylcarboxylic acid functionalized SBA-CO_2H (1/9) was prepared by heating SBA-CN (1/9) (4 g, 6.1 mmol) under reflux with an aqueous solution of H_2SO_4 (100 mL, 50%) at 120 °C over 12 h. The solid product, SBA-CO_2H (1/9), was recovered by filtration, washed several times with water, ethanol, acetone and diethyl ether and then dried at 70 °C under vacuum.[27]

Sample Hydration: The samples were dehydrated at 80 °C for 24 h and then brought into contact with a water saturated atmosphere for 24 h at room temperature.

X-ray Diffraction (XRD): The powder X-ray diffraction patterns were recorded with a X-PERT PRO II Philips diffractometer by using Cu-K_α radiation (λ = 1.54056 Å).

Transmission Electron Microscopy (TEM): The TEM observations were carried out at 100 kV with a JEOL 1200 EXII microscope. The samples for the TEM measurements were prepared by using ultramicrotomy techniques and were then deposited on the copper grids.

Nitrogen Adsorption and Desorption Isotherms: The nitrogen adsorption and desorption isotherms were measured at 77 K with a Micromeritics TRISTAR 3000 analyzer. Before these measurements were performed, the samples were outgassed for 12 h at 70 °C under a stable vacuum of 4×10^{-3} mbar. The Brunauer–Emmett–Teller (BET) specific surface area was evaluated by using the adsorption data in a relative pressure range of 0.04 to 0.20, where the BET equation is applicable.[71] The mesopore size distribution was calculated on the basis of the desorption branches of the nitrogen isotherms by using the Barrett–Joyner–Halenda method (BJH)[72] and the pore size (D_p) was obtained from the peak position of the distribution curve. The total pore volume was determined from the amount that was adsorbed at a relative pressure of approximately 0.97. The micropore volumes were assessed by means of a t-plot analysis, for which the Harkins and Jura's expression was used to calculate the adsorbed layer thickness.[73]

Solid-State NMR: The solid state NMR spectra were recorded with a Varian VNMRS 400 Solid spectrometer with a magnetic field strength of 9.4 T and that was equipped with a 7.5 mm and a 3.2 mm MAS probe. The 7.5 mm MAS probe was used for the ^{29}Si and ^{13}C nuclei with a spinning rate of 5 kHz. The 3.2 mm MAS probe was used for the ^{31}P nucleus with a spinning rate of 10 kHz. Single pulse sequences with continuous decoupling were used for the ^{29}Si NMR experiment with a 5 µs $\pi/2$ pulse duration and a recycle delay of 60 s. The same spectral decomposition was obtained with a 200 s recycle delay. This enabled us to propose that in our materials the ^{29}Si experiments that were recorded with a recycle delay of 60 s were quantitative. The CP MAS experiments for the ^{13}C nucleus were acquired with a 5 s pulse sequence repetition delay, a 5 µs $\pi/2$ (^1H) pulse duration and a 3 ms contact time. Single pulse sequences with tppm[74] decoupling were used for the ^{31}P NMR spectroscopy experiment with a 4 µs $\pi/2$ pulse duration and a recycle delay of 30 s. The ^{29}Si and ^{13}C nuclei were referenced to tetramethylsilane (TMS). The ^{31}P nucleus was referenced to H_3PO_4. The solid state NMR spectra were fitted by using the Dmfit program.[75]

Differential Scanning Calorimetry (DSC): A Netzsch DSC 204 F1 was used for the DSC measurements under a N_2 flux from –150 to 425 °C and with a heating rate of 2 °C/min.

Complex Impedance Spectroscopy (CIS): The proton conductivity was measured by CIS. The isothermal conductivity measurements were performed over a frequency range of 10^{-2} to 10^6 Hz with a Novocontrol dielectric alpha analyzer. The temperature of the sample, which ranged from –100 to 70 °C, was controlled by a Quatro Novocontrol system. In order to prevent any destruction of the silica porous structure under external pressure, the conductivity measurements were not carried out on the pellets that had been prepared from the compressed powder. Instead, we employed a specific cell that was similar to that generally used for liquids. The powder sample (approximately 100 mg) was poured onto the lower electrode of the cell and then, very gently, pressed by the upper metallic electrode. CIS gives access to the real part of the a.c. conductivity, which results, in many cases, from the superposition of the Maxwell–Wagner–Sillars contribution $\sigma_{MWS}(\omega,T)$, the d.c. con-

ductivity, $\sigma_{dc}(T)$ and the polarization conductivity, $\sigma_{pol}(\omega,T)$; see Equation (7).

$$\sigma_{ac}(\omega,T) = \sigma_{MWS}(\omega,T) + \sigma_{dc}(T) + \sigma_{pol}(\omega,T) \quad (7)$$

Basically, the d.c. conductivity corresponds to the long-range redistribution of the charges, that is ionic or electron transport, while the polarization contribution arises from the local rearrangement of the charges or the dipoles that causes dipolar reorientation and thus results in the intrinsic bulk polarization. The Maxwell–Wagner–Sillars polarization is due to the accumulation of the charges at the sample/electrode interface and also depends on extrinsic parameters, such as the sample shape.

Supporting Information (see footnote on the first page of this article): Additional information as noted in the text.

[1] K. J. Shea, D. A. Loy, *Chem. Rev.* **1995**, *95*, 1431–1442.
[2] R. J. P. Corriu, *Angew. Chem.* **2000**, *112*, 1432; *Angew. Chem. Int. Ed.* **2000**, *39*, 1376–1398.
[3] R. J. P. Corriu, *Eur. J. Inorg. Chem.* **2001**, *5*, 1109–1121.
[4] J. S. Beck, J. C. Vartuli, W. J. Roth, M. E. Leonowicz, C. T. Kresge, K. D. Schmitt, C. T. W. Chu, D. H. Olson, E. W. Sheppard, *J. Am. Chem. Soc.* **1992**, *114*, 10834–10843.
[5] C. Sanchez, B. Julian, P. Belleville, M. Popall, *J. Mater. Chem.* **2005**, *15*, 3559–3592.
[6] A. Walcarius, L. Mercier, *J. Mater. Chem.* **2010**, *20*, 4478–4511.
[7] A. Kuschel, S. Polarz, *J. Am. Chem. Soc.* **2010**, *132*, 6558–6565.
[8] L. Mercier, T. J. Pinnavaia, *Adv. Mater.* **1997**, *9*, 500–503.
[9] A. Cauvel, G. Renard, D. Brunel, *J. Org. Chem.* **1997**, *62*, 749–751.
[10] P. M. Price, J. H. Clark, D. J. Macquarrie, *J. Chem. Soc., Dalton Trans.* **2000**, *2*, 101–110.
[11] S. L. Burkett, S. D. Sims, S. Mann, *Chem. Commun.* **1996**, 1367–1368.
[12] A. Walcarius, C. Delacôte, *Chem. Mater.* **2003**, *15*, 4181–4192.
[13] D. J. Macquarrie, *Chem. Commun.* **1996**, 1961–1962.
[14] R. J. P. Corriu, C. Hoarau, A. Mehdi, C. Reye, *Chem. Commun.* **2000**, 71–72.
[15] S. Mikhailenko, D. Desplantier-Giscard, C. Danumah, S. Kaliaguine, *Microporous Mesoporous Mater.* **2002**, *52*, 29–37.
[16] D. Margolese, J. A. Melero, S. C. Christiansen, B. F. Chmelka, G. D. Stucky, *Chem. Mater.* **2000**, *12*, 2448–2459.
[17] R. Marschall, I. Bannat, J. Caro, M. Wark, *Microporous Mesoporous Mater.* **2007**, *99*, 190–196.
[18] R. Marshall, J. Rathousky, M. Wark, *Chem. Mater.* **2007**, *19*, 6401–6407.
[19] J. Wu, Z. Cui, C. Zhao, H. Li, Y. Zhang, T. Fu, H. Na, W. Xing, *Int. J. Hydrogen Energy* **2009**, *34*, 6740–6748.
[20] Y. G. Jin, S. Z. Qiao, Z. P. Xu, Z. Yan, Y. Huang, J. C. Diniz da Costa, G. Q. Lu, *J. Mater. Chem.* **2009**, *19*, 2363–2372.
[21] Y. G. Jin, S. Z. Qiao, Z. P. Xu, J. C. Diniz da Costa, G. Q. Lu, *J. Phys. Chem. C* **2009**, *113*, 3157–3163.
[22] R. Supplit, A. Sugawara, H. Peterlik, R. Kikuchi, T. Okubo, *Eur. J. Inorg. Chem.* **2010**, 3993–3999.
[23] S. J. Paddison, K. D. Kreuer, J. Maier, *Phys. Chem. Chem. Phys.* **2006**, *8*, 4530–4542.
[24] H. Steininger, M. Schuster, K. D. Kreuer, A. Kaltbeitzel, B. Bingol, W. H. Meyer, S. Schauff, G. Brunklaus, J. Maier, H. W. Spiess, *Phys. Chem. Chem. Phys.* **2007**, *9*, 1764–1773.
[25] R. J. P. Corriu, E. Lancelle-Beltran, A. Mehdi, C. Reye, S. Brandes, R. Guilard, *J. Mater. Chem.* **2002**, *12*, 1355–1362.
[26] R. Mouawia, A. Mehdi, C. Reyé, R. J. P. Corriu, *J. Mater. Chem.* **2008**, *18*, 4193–4203.
[27] B. Folch, J. Larionova, Y. Guari, C. Guerin, A. Mehdi, C. Reyé, *J. Mater. Chem.* **2004**, *14*, 2703–2711.
[28] R. J. P. Corriu, L. Datas, Y. Guari, A. Mehdi, C. Reyé, C. Thieuleux, *Chem. Commun.* **2001**, 763–764.
[29] D. Y. Zhao, Q. S. Huo, J. L. Feng, B. F. Chmelka, G. D. Stucky, *J. Am. Chem. Soc.* **1998**, *120*, 6024–6036.
[30] J. Alauzun, A. Mehdi, C. Reyé, R. J. P. Corriu, *New J. Chem.* **2007**, *31*, 911–915.
[31] D. H. Everett in *The Structure and Properties of Porous Materials* (Eds.: D. H. Everett, F. S. Stone), Butterworths, London, **1958**, p. 116–128.
[32] P. Van Der Voort, P. I. Ravikovitch, K. P. De Jong, M. Benjelloun, E. Van Bavel, A. H. Janssen, A. V. Neimark, B. M. Weckhuysen, E. F. Vansant, *J. Phys. Chem. B* **2002**, *106*, 5873–5877.
[33] J. W. McBain, *J. Am. Chem. Soc.* **1935**, *57*, 699–700.
[34] R. J. P. Corriu, E. Lancelle-Beltran, A. Mehdi, C. Reye, S. Brandes, R. Guilard, *J. Mater. Chem.* **2002**, *12*, 1355–1362.
[35] A. Aliev, D. L. Ou, B. Ormsby, A. C. Sullivan, *J. Mater. Chem.* **2000**, *10*, 2758–2764.
[36] X. G. Wang, S. F. Cheng, J. C. C. Chan, *J. Phys. Chem. C* **2007**, *111*, 2156–2164.
[37] R. J. P. Corriu, L. Datas, Y. Guari, A. Mehdi, C. Reyé, C. Thieuleux, *Chem. Commun.* **2001**, 763–764.
[38] J. Alauzun, A. Mehdi, C. Reye, R. J. P. Corriu, *J. Mater. Chem.* **2007**, *17*, 349–356.
[39] D. Molero, J. Coro, R. Perez, M. Suarez, R. Martinez-Alvarez, A. Herrera, N. Martin, *Magn. Reson. Chem.* **2007**, *45*, 93–98.
[40] P. M. Tolstoy, P. Schah-Mohammedi, S. N. Smirnov, N. S. Golubev, G. S. Denisov, H. H. Limbach, *J. Am. Chem. Soc.* **2004**, *126*, 5621–5634.
[41] I. Diaz, C. Marquez-Alvarez, F. Mohino, J. Perez-Pariente, E. Sastre, *J. Catal.* **2000**, *193*, 283–294.
[42] G. Morales, G. Athens, B. F. Chmelka, R. van Grieken, J. A. Melero, *J. Catal.* **2008**, *254*, 205–217.
[43] G. J. D. Soler-Illia, C. Sanchez, B. Lebeau, J. Patarin, *J. Chem. Rev.* **2002**, *102*, 4093–4138.
[44] N. Fekkar-Nemmiche, S. Devautour-Vinot, B. Coasne, F. Henn, A. Mehdi, C. Reye, R. Corriu, *Eur. Phys. J. Special Top.* **2007**, *141*, 45–48.
[45] L. D. Gelb, K. E. Gubbins, R. Radhakrishnan, M. Sliwinska-Bartkowiak, *Rep. Prog. Phys.* **1999**, *62*, 1573–1659.
[46] A. Schreiber, I. Ketelsen, G. H. Findenegg, *Phys. Chem. Chem. Phys.* **2001**, *3*, 1185–1195.
[47] K. Morishige, K. Kawano, *J. Chem. Phys.* **1999**, *110*, 4867–4872.
[48] K. Morishige, H. Iwasaki, *Langmuir* **2003**, *19*, 2808–2811.
[49] K. Morishige, H. Yasunaga, Y. Matsutani, *J. Phys. Chem. C* **2010**, *114*, 4028–4035.
[50] R. Evans, *J. Phys. Condens. Matter* **1990**, *2*, 8989–9007.
[51] S. Jähnert, F. Vaca Chavez, G. E. Schaumann, A. Schreiber, M. Schönhoff, G. H. Findenegg, *Phys. Chem. Chem. Phys.* **2008**, *10*, 6039–6051.
[52] I. Brovchenko, A. Oleinikova, *Interfacial and Confined Water*, Elsevier, Amsterdam, **2008**.
[53] M. Brun, A. Lallemand, J. F. Quinson, C. Eyraud, *Thermochim. Acta* **1977**, *21*, 59–88.
[54] G. H. Findenegg, S. Jähnert, D. Akcakayiran, A. Schreiber, *ChemPhysChem* **2008**, *9*, 2651–2659.
[55] F. Kremer, A. Schönhals, *Broadband dielectric spectroscopy*, Springer, Berlin, Heidelberg, New York, **2003**.
[56] A. Spanoudaki, B. Albela, L. Bonneviot, M. Peyrard, *Eur. Phys. J. E* **2005**, *17*, 21–27.
[57] J. Banys, M. Kinka, J. Macutkevic, G. Völkel, W. Böhlmann, V. Umamaheswar, M. Hartmann, A. Pöppl, *J. Phys. Condens. Matter* **2005**, *17*, 2843–2857.
[58] M. Sliwinska-Bartkowiak, J. Gras, R. Sikorski, R. Radhakrishnan, L. Gelb, K. E. Gubbins, *Langmuir* **1999**, *15*, 6060–6069.
[59] Y. Ryabov, A. Gutina, V. Arkhipov, Y. Feldman, *J. Phys. Chem. B* **2001**, *105*, 1845–1850.
[60] J. Dore, B. Webber, M. Hartl, P. Behrens, T. Hansen, *Phys. A* **2002**, *31*, 501–507.
[61] E. Liu, J. C. Dore, J. B. Webber, D. Khushalani, S. Jahnert, G. H. Findenegg, T. Hansen, *J. Phys. Condens. Matter* **2006**, *18*, 10009–10028.

[62] C. J. D. von Grotthuss, *Ann. Chim.* **1806**, *58*, 54–58.
[63] K. D. Kreuer, A. Rabenau, W. Weppner, *Angew. Chem.* **1982**, *94*, 224; *Angew. Chem. Int. Ed. Engl.* **1982**, *21*, 208–209.
[64] N. Agmon, *J. Phys. Chem. B* **1997**, *101*, 4352–4352.
[65] B. Grunberg, T. Emmler, E. Gedat, I. Shenderovich, G. H. Findenegg, H. H. Limbach, G. Buntkowsky, *Chem. Eur. J.* **2004**, *10*, 5689–5696.
[66] I. K. Mbaraka, B. H. Shanks, *J. Catal.* **2006**, *244*, 78–85.
[67] J. M. Rosenholm, T. Czuryszkiewicz, F. Kleitz, J. B. Rosenholm, M. Linden, *Langmuir* **2007**, *23*, 4315–4323.
[68] S. W. Ong, X. L. Zhao, K. B. Eisenthal, *Chem. Phys. Lett.* **1992**, *191*, 327–335.
[69] L. D. Freedman, G. O. Doak, *Chem. Rev.* **1957**, *57*, 479–523.
[70] S. Jansat, K. Pelzer, J. Garcia-Anton, R. Raucoules, K. Philippot, A. Maisonnat, B. Chaudret, Y. Guari, A. Mehdi, C. Reye, R. J. P. Corriu, *Adv. Funct. Mater.* **2007**, *17*, 3339–3347.
[71] K. S. W. Sing, D. H. Everett, R. A. W. Haul, L. Moscou, R. A. Pierotti, J. Rouquerol, T. Siemieniewska, *Pure Appl. Chem.* **1985**, *57*, 603–619.
[72] E. P. Barrett, L. G. Joyner, P. P. Halenda, *J. Am. Chem. Soc.* **1951**, *73*, 373–380.
[73] G. Jura, W. D. Harkins, *J. Chem. Phys.* **1943**, *11*, 430–431.
[74] A. E. Bennett, C. M. Rienstra, M. Auger, K. V. Lakshmi, R. G. Griffin, *J. Chem. Phys.* **1995**, *103*, 6951–6958.
[75] D. Massiot, F. Fayon, M. Capron, I. King, S. Le Calve, B. Alonso, J. O. Durand, B. Bujoli, Z. H. Gan, G. Hoatson, *Magn. Reson. Chem.* **2002**, *40*, 70–76.

Received: February 23, 2011
Published Online: June 15, 2011

